CuO improved $(Sn,Sb)O_2$ ceramic anodes for electrochemical advanced oxidation processes

María-José Sánchez-Rivera[a], Juan José Giner-Sanz[b], Valentín Pérez-Herranz[b] Sergio Mestre[a,c]

[a] University Institute of Ceramic Technology, Universitat Jaume I, 12006 Castellón, Spain.
[b] IEC Group, Department of Chemical and Nuclear Engineering, Universitat Politècnica de València, 46022 Valencia, Spain.
[c] Department of Chemical Engineering. Universitat Jaume I,12006 Castellón, Spain.

Corresponding author's e-mail address: mariajose.sanchez@itc.uji.es

Abstract

Antimony-doped tin oxide electrodes with copper oxide as sintering aid are presented as an economical and easily manufactured alternative to metal-based electrodes, intended for the electrooxidation process of emerging and recalcitrant organic contaminants in wastewaters. The CuO proportion has been optimized to obtain densified electrodes with a mild thermal cycle (T_{max} = 1200 °C). One of the manufactured electrodes (97.8 mol.% of SnO_2, 1.0 mol.% of Sb_2O_3 and 1.2 mol.% of CuO) was selected for electrochemical characterization from a physical and morphological analysis. The electrochemical behavior of the selected electrode showed that the addition of CuO as sintering aid widens the electrochemical window and increases the electrode "inactivity", with respect to an $(Sn, Sb)O_2$ electrode synthesized in the same conditions. In return, the $(Sn,Sb,Cu)O_2$ electrode presents a significantly lower electrochemical rugosity factor. Moreover, the addition of CuO does not change the OER mechanism, but it modifies the kinetic parameters, leading to a larger accumulation of hydroxyl radicals. Consequently, the addition of CuO as sintering aid significantly improves the electrochemical properties of the electrode as an EAOP anode with respect to the $(Sn,Sb)O_2$ electrode, at the expense of worsening its electrochemical roughness factor. The results of the electrochemical characterization were confirmed by Norfloxacin degradation tests.

Keywords
Sintering, Electrodes, Electrical conductivity, Oxidation process

1 Introduction

In the last years, electrooxidation has been one of the processes that has attracted more attention in the field of recalcitrant organic compound elimination from industrial wastewaters (1). In this process, high-cost electrodes are frequently used as anodes, on which the chemical reaction that oxidizes complex organic compounds to simpler ones takes place. The ultimate aim is the complete mineralization of the organic pollutants. The most known electrodes are based on titanium oxides Ti_nO_{2n-1} (n from 4 to 10) (2–4), indium-doped tin oxide (ITO) (5,6) and fluorine-doped tin oxide (FTO) (7)**.** However, these present some important limitations. On the one hand, the high cost owing to some scarce elements or the difficulty of the processing. On the other hand, in most of the described applications, the electrode is manufactured as a thin layer on a conductive substrate that withstands the chemical attack (titanium, platinum). These metal-supported electrodes have been extensively researched, but the electrochemical behavior of electrodes constituted solely by conductive ceramics have received less attention.

Antimony-doped tin oxide can be an alternative to synthesize electrodes for electrooxidation because it is cheaper and more easily manufactured (8). Tin oxide is a n-type semiconductor used in a wide range of chemical and electronic industrial applications (9–15). However, it is necessary to improve its electrical conductivity to make it suitable for manufacturing electrodes. There are numerous references about dopants which increase the electrical conductivity of SnO_2, but antimony oxide offers a good relation performance/cost. In fact, in a previous work, the effectiveness of an antimony-doped tin oxide anode in the degradation of an antibiotic by electrooxidation was demonstrated (16). Despite this fact, the nearly zero densification of these electrodes make them fragile and not suitable for industrial testing.

It is well known that one of the main difficulties in manufacturing ceramic SnO_2-based electrodes is its poor sinter ability (17)**.** This drawback is usually counteracted, either by the application of special sintering techniques (18–22), as the "field activated sintering technique" (FAST) (23), or by using “sintering aids”, as CuO, ZnO, MnO_2, between many others (24,25). Copper oxide was chosen as sintering aid by its moderate cost and because it has been successfully tested in SnO_2-based anodes for the aluminum production process (26–30).

This work was focused on improving the mechanical behavior of already tested antimony-doped tin oxide electrodes to make them suitable for industrial scaling without losing their performance as anode in electrooxidation processes. A series of (Sb,Sn,Cu)O_2 electrodes with different CuO contents, was synthetized. The electrodes were characterized from a physical and morphological point of view. The electrode with the best compromise between densification and resistivity was selected for a complete electrochemical characterization. Several parameters that are relevant for evaluating the performance of the electrode as an electrochemical advanced oxidation process (EAOP) anode, were determined: the electrochemical window, the electrochemical rugosity factor, and the oxygen evolution reaction (OER) Tafel parameters. The results were compared with analogue data obtained for an "active" anode (i.e. Pt), for an actual state-of-the-art "inactive" anode (i.e. BDD), and for a copper-free (Sb,Sn)O_2 anode sintered in the same conditions. Moreover, in order to confirm the electrochemical characterization results, degradation tests were performed for a model organic recalcitrant pollutant. In this work, Norfloxacin (NOR) was selected as model pollutant, since it is one of the organic recalcitrant pollutants that have been extensively studied in literature.

2 Experimental procedure

2.1. Electrode synthesis and physical characterization

Electrode's raw materials were SnO_2 (purity 99.85%, Quimialmel S.A., Castellón, Spain), Sb_2O_3 as dopant (purity 99%, Alfa-Aesar, Germany) and CuO as sintering aid (purity 97%, Panreac S.A., Spain). Eight compositions were tested with different proportions of copper oxide (Table 1). Each of them included an additional 0.8 wt.% of polyvinylalcohol (Mowiol 8-88, Clariant Iberica S.A. Barcelona, Spain), as a ligand.

The electrodes were obtained through the traditional ceramic method (no special technique was employed for shaping or sintering the specimens). The raw materials were mixed using water as a fluid in a planetary mill working at 230 rpm for one hour (Pulverisette 5, Fritsch GmbH, Germany). The obtained suspension was dried in an oven at 110°C for 24 h. The dry powder was sieved trough a 600 μm mesh and moistened to 5.0 % (kg water/kg dry solid). Prismatic specimens of 40x5x5 mm were shaped by dry pressing in a laboratory uniaxial manual press

(Robima S.A., Valencia, Spain), working at 250 $kg \cdot cm^{-2}$. Finally, the samples were sintered in a laboratory furnace (RHF1600, Carbolite Gero Limited, Hope Valley, UK). The thermal cycle had three stages, heating at 5 $°C \cdot min^{-1}$ up to 1200 °C, one hour of soaking time at 1200 °C and cooling. At least three specimens were sintered in each cycle.

Bulk density of green and sintered specimens was measured by mercury immersion (Archimedes' method), and their densification (Ψ) was calculated as the change in bulk density due to sintering divided by the change needed to attain a pore-free solid, according to German (31)**.** The pore size distribution as well as the total pore volume of the electrodes was measured through the mercury intrusion porosimetry technique (AutoPore IV 9500, Micromeritics, USA) and the microstructure was visualized by FEG-SEM (QUANTA 200F, FEI Co, USA) in polished sections of selected samples. Finally, the electrical resistivity of sintered samples was measured with a resistance meter (RM 3545, Hioki E.E. Corp. Japan), taking the average of ten measures for each specimen.

2.2. Electrochemical characterization

Four electrodes were considered in the electrochemical characterization: a copper-free $(Sn,Sb)O_2$ electrode (composition A), the $(Sb,Sn,Cu)O_2$ electrode selected after the physical and morphological analysis, a mirror polished Pt electrode, and a commercial 2500 ppm Nb-supported BDD electrode (Neocoat SA, La chaux de Fonds, Switzerland). The electrochemical characterization of the electrodes was carried out in a conventional 3-electrode thermostated electrochemical cell, using a 302N Autolab® potentiostat/galvanostat with FRA module, controlled with NOVA® software (Metrohm Autolab B.V., Utrecht, The Netherlands). The electrode to be characterised was used as working electrode. Before starting the electrochemical test, its geometric surface was precisely measured using a confocal laser scanning microscope (Olympus® LEXT OLS 3000, Olympus Europa SE & Co. KG, Hamburg, Germany). A commercial Pt ring electrode (Crison® 5267) was used as counter-electrode, and a commercial Ag/AgCl (3M KCl) electrode (Crison® 5240, HACH LANGE SPAIN, S.L.U., Barcelona, Spain) was used as reference electrode. All the experiments were done at 30°C, using a 0.1 M Na_2SO_4 (Panreac S.A., Spain) electrolyte.

First, cyclic voltametries (CVs) were performed in the anodic domain at 10 different scan rates, equally spaced from 100 $mV \cdot s^{-1}$ to 10 $mV \cdot s^{-1}$. Each voltammetry was carried out from the open circuit potential (OCP) to +4V. For each scan rate, 30 cycles were measured in order to ensure the convergence to the corresponding limit cycle. Then, the pseudo-steady-state polarization curve was measured from OCP to +4V, at 1 $mV \cdot s^{-1}$, since as it was observed in preliminary studies, that scan rate is slow enough to reach the steady-state in each point. Second, the electrochemical impedance spectrum (EIS) was measured at 15 different overpotentials. EIS is an electrochemical technique that has been applied to a wide range of applications (32)(33). Its main strength is that it allows to deconvolve the different physic-chemical processes undergoing at different timescales in the system (34). In this work, EIS was used to obtain the uncompensated resistance of the system at different overpotentials, in order to correct the ohmic drop in the measured CVs. The main limitation of EIS is that its validity is restricted to situations in which causality, linearity and stability are achieved (35). For this reason, validation is a fundamental part of the preliminary analysis of experimental EIS spectra. In this work, all the measured EIS spectra were double-validated: on the one hand, they were validated using the linearity assessment methods developed in previous works (36)(37); on the other hand, they were validated using the Kramers-Kronig based quantitative validation technique described elsewhere (38)(39). The EIS measurements were performed at 100 frequencies logarithmically spaced between 10 kHz and 10 MHz. The measurement parameters were selected using the methodology presented in a previous work (40). Finally, since electrochemical systems are highly nonlinear (41)(42), the proper selection of the perturbation amplitude is crucial for fulfilling the linearity hypothesis. In this research, a perturbation amplitude of 20 mV was used for all the EIS measurements. This amplitude was selected using the selection methodology presented in previous works (43)(44).

The uncompensated resistance is given by the high frequency intersect of the EIS spectrum with the real axis (45): in this work, the uncompensated resistance for each overpotential was determined from the high frequency intersect of the experimentally measured impedance spectrum for that overpotential with the real axis. Both, the CVs and the pseudo-steady-state polarization curve, were I-R corrected using the procedure described by Hrbac and co-workers (46), and the uncompensated resistances determined from EIS measurements.

Finally, the NOR degradation tests were performed using 100 $mg \cdot L^{-1}$ NOR (Sigma-Aldrich) solutions, containing 2 $g \cdot L^{-1}$ of Na_2SO_4 as supporting electrolyte. These degradation tests were carried out in a 250 cm^3 cylindrical electrochemical reactor, at room temperature, for four hours. The cathode was a 20 cm^2 AISI 304 stainless steel sheet, while the anode was the electrode that was going to be characterized: either one the ceramic electrodes (i.e. the $(Sn,Sb)O_2$ electrode or the $(Sb,Sn,Cu)O_2$ electrode) or a BDD electrode (NewCoat®), all of them with a geometric surface area of 12 cm^2. A commercial Ag/AgCl (3M KCl) electrode (Crison® 5240) was used as reference electrode to measure the anodic electrode potential. The degradation tests were all done in galvanostatic mode at an applied current density of 80 $mA \cdot cm^{-2}$, using a DC power supply. Samples were taken from the electrochemical reactor every 30 min. The electrode potential, the cell voltage and the current were monitored throughout the whole degradation test. The NOR degradation was monitored by measuring the variation of the absorbance at 275 nm using an Unicam UV4-200 UV/vis spectrometer (Pye Unicam, Cambridge, UK). Finally, the NOR mineralization was monitored trough the total organic carbon (TOC) measured using a Shimadzu TNM-L ROHS TOC analyzer.

3 Experimental results and discussion

3.1. Physical and morphological analysis

The weight loss of the specimens after the sintering thermal cycle was around the 0.8 %, which was the expected value considering the percentage of PVA in each sample. However, the distribution was not aleatory in function of the CuO content (Figure 1). It seems that moderate percentages of copper oxide exert a subtle effect, reducing the weight loss. A hypothesis can be proposed to interpret this behaviour, taking into account the mass changes associated with CuO $\rightarrow Cu_2O$ reduction (-10.06 wt.%) and $Sb_2O_3 \rightarrow Sb_2O_5$ oxidation (+10.98 wt.%). Said reactions can take place in the $CuO\text{-}Sb_2O_3$ system at high temperatures according to Stan et al. (47). The estimation of the mass loss according to whether each or both reactions operates simultaneously covers approximately the range of experimental data, as is also shown in Figure 1. Consequently, the progressive addition of CuO to the mixture would facilitate the course of both reactions, although the effect would not be linear but linked to the proportion of CuO, reaching the minimum

in mass loss when CuO and Sb_2O_3 are equimolar in the composition. A further increase in the proportion of CuO would already entail a growth in mass loss, as predicted by the estimate.

By contrast, the addition of copper oxide has a significant impact over densification (Figure 2). The sigmoidal trend has its maximum slope for CuO contents around 1 mol.%, interval where the weight loss is the lowest. In consequence, copper oxide contents lower than 0.5 mol.% do not allow the densification of the samples with the selected thermal cycle, but contents higher than 1.2 mol.% generates nearly full-densified samples ($\Psi \approx 95$ %). In addition, the measurements of the samples in the critical interval showed a higher variability, which means that small changes in the processing (as the position of the specimen in the furnace coupled with a small temperature gradient in the chamber), can have some effects on the final properties of the specimen. According to Lalande et al. (48), CuO addition facilitates a grain-boundary mass transport mechanism for sintering at moderate temperature (< 1050 °C), and, a higher temperature, the eutectic liquid formed in the CuO-Cu_2O system (1090 °C) may also contribute through a liquid phase mass transport mechanism. However, Zhang et al. suggested that densification is mainly due to a viscous flow mechanism, facilitated by the formation of disordered Cu-containing amorphous-like layers in the surface of the particles (49). The two hypotheses are compatible with the need of a minimum quantity of copper oxide to achieve a high densification, but do not explain the subtle effect of CuO over the weight loss.

SEM micrographs of sintered specimens of compositions A and G (Figure 3) showed big differences in microstructure, coherent with their densification values and their pore size distributions (Figure 4 and Table 2). The specimens of composition A were constituted by an open and highly porous network of interconnected submicronic particles, as shows its total pore volume of 0.075 $cm^3.g^{-1}$, with a pore size distribution centered around a diameter of 0.2 µm. By contrast, composition G's specimens showed some rounded and isolated pores inside a body formed by well sintered micrometer-sized grains. This microstructure is consistent with the virtually zero total pore volume obtained in the mercury intrusion test. No signs of accumulations of antimony oxide or copper oxide were detected in any of the samples, which pointed to a good homogenization of the added CuO and Sb_2O_3. Obviously, the CuO addition promotes grain and pore growth, along with a reduction in total porosity, which improves the mechanical properties of specimens (the

copper-free specimens were very fragile, but the copper-rich ones have good mechanical strength).

In opposition to the improvement of mechanical properties, copper oxide has an unfavourable effect over electrical resistivity, since the lowest value of this property was obtained with composition B specimens (with the smallest proportion of CuO, Figure 5), but it was only a little lower than the copper-free specimens (composition A). Additions of copper oxide in proportions higher than 0.1 mol.% provokes a progressive increase in the resistivity, except around the compositions which correspond with the maximum slope at densification curve (1 mol.%). In this range, resistivity showed a clear peak which deviates from the general trend. As a hypothesis, it can be proposed that this behaviour is related with the properties of the intergranular phases responsible of the densification mechanism, whose proportion must be higher in the specimens corresponding to this interval of composition and sintered with the employed thermal treatment.

Results showed that nearly fully-densified Sb-doped electrodes could be obtained by incorporating CuO as a sintering aid in proportions higher than 1 mol.%, although at the expense of raising the resistivity. However, the obtained values, around 1 Ω·cm, allows the use of the specimens as electrodes for electrooxidation. Composition “G”, (1.2 mol.% in CuO) was considered a compromise between high densification and low resistivity. In consequence, the electrodes with composition G were chosen to carry on their electrochemical characterization.

3.2. Electrochemical characterization

Figure 6 presents the I-R corrected CVs obtained at a scan rate of 100 $mV \cdot s^{-1}$. Figure 6.a represents the current density referred to the geometric area versus the applied potential; whereas figure 6.b represents the current density referred to the active surface versus the applied potential. As it can be observed in figure 6.a, for a given applied potential, the geometric current density of the BDD anode is the lowest, and the geometric current density of the Pt anode is the biggest. The ceramic anodes present intermediate geometric current densities. Comparing them, at a given applied potential, the $(Sn,Sb)O_2$ presents a larger geometric current density than the $(Sn,Sb,Cu)O_2$ anode. The current densities referred to the active surface display the same trends,

as it can be seen in figure 6.b. This shows that the differences observed in the geometric current densities cannot be fully explained by the difference in the electrochemical rugosity factor of the different anodes. Consequently, the four anodes present different OER intrinsic activities. For the sake of clarity, in this work only the CVs obtained for one of the scan rates (100 $mV \cdot s^{-1}$) are presented. However, the trends observed for 100 $mV \cdot s^{-1}$ were also observed in the other 9 scan rates.

From the observations, several ideas can be extracted. First, the well-known fact that the Pt electrode is the most "active" anode among the 4 considered electrodes, and the BDD electrode is the most "inactive" one. Second, the ceramic electrodes present intermediate activities. Comparing the two ceramic electrodes between them, the $(Sn,Sb,Cu)O_2$ anode is significantly more "inactive" than the $(Sn, Sb)O_2$ one. Therefore, the addition of CuO (1.2 mol.%) decreases the intrinsic activity of the ceramic electrode, making its electrochemical behavior more similar to the BDD's one. A lower anode activity leads to a higher accumulation of strong oxidizing OER intermediates (v.g. hydroxyl radicals); and therefore, favors the organic compound mineralization (50). Hence, the addition of CuO (1.2 mol.%) improves the electrochemical behavior as an EAOP anode of the $(Sn,Sb)O_2$ ceramic electrode.

Figure 7 gives the OCP of the different anodes. There is no significant difference between the OCP of the $(Sn,Sb,Cu)O_2$ electrode, and the one of the $(Sn,Sb)O_2$ electrode; which, in turn, are significantly higher than the OCPs of the Pt electrode and the BDD electrode. This indicates that the addition of CuO (1.2 mol.%) does not significantly change the open-circuit electrochemical behavior of the anode. This observation is expectable since the added Cu quantity is relatively small, and thus, the chemical composition of the anode surface is relatively similar in both ceramic electrodes.

Another important parameter for accessing the performance of a given electrode as an EAOP anode is its electrochemical rugosity factor (γ). This factor is defined as the ratio of the real active surface and the geometric area. In this work, the following expression was used to calculate the γ factor of the considered ceramic electrodes (Equation 1 in Appendix 1).

Where Q_{out} denotes the “outer” charge, related to the more accessible surface; while, Q_{in} denotes the "inner" charge, relayed to the less accessible surface. The “total” charge (Q_{total}) is defined as the sum of the two charges. In this work, Q_{out} and Q_{in} were determined for each electrode using the Ardizzone’s method (51) and the voltammetric charge analysis of the CVs measured at 10 different scan rates.

Figure 8 shows the electrochemical rugosity factor obtained for each one of the ceramic electrodes. It can be observed that the (Sn,Sb,Cu)O_2 electrode has a γ factor 20% lower than the (Sn, Sb)O_2 electrode. Therefore, the addition of CuO (1.2 mol.%) has a significant negative effect on the electrochemical rugosity of the anode. These electrochemical rugosity factor values are consistent with the microstructures of both electrodes (figure 3). Since the common practice in electrochemistry is to try to maximize the active surface for a given geometric area, the addition of CuO worsens the performance of the ceramic electrode with respect to its active surface.

Figure 9 presents the I-R corrected pseudo-steady-state polarization curves. The trends observed in this figure are the same trends that were observed in the CVs (figure 6). This reinforces the hypothesis on the activity of the different anodes, proposed from the CVs. An important parameter that can be extracted from the steady-state polarization curves is the oxygen evolution potential (OEP). Its importance is due to the fact that it defines the electrochemical window of the electrode. This parameter corresponds with the potential from which the generation of oxygen becomes significant. Since this definition is a rather fuzzy definition, the common practice is to define it as the intersection of the tangent to the steady-state polarization curve at high anodic potentials, and the applied potential axis. Using this definition, the OEP was determined for each electrode: the corresponding tangents are shown as dotted lines in figure 9. Figure 10 gives the OEP for each one the electrodes considered in this work. The OEP values determined in this work for the Pt electrode (52), for the BDD electrode and for the ceramic electrodes (16), are consistent with the values available in literature for similar electrodes.

The Pt electrode has the lowest OEP among the 4 electrodes, while the BDD electrode has the highest. The ceramic electrodes present intermediate OEPs. Comparing both ceramic electrodes, the (Sn,Sb,Cu)O_2 electrode has a significantly higher OEP than the (Sn,Sb)O_2 electrode: the addition of CuO (1.2 mol.%) leads to a 38% raise in the OEP, though the OEP of the (Sn,Sb,Cu)O_2 electrode is still significantly lower than the BDD's one. It is well-known that in the EAOP context, wide electrochemical windows (i.e. high OEP) are sought (53)(54). Consequently, the addition of CuO (1.2 mol.%) improves the performance of the ceramic electrode as an EAOP anode, in terms of its electrochemical window.

Figure 11 presents the I-R corrected pseudo-steady-state polarization curves in the Tafel plane: overpotential (η) versus $\log_{10}$(i). The first observation that can be extracted from figure 11 is that both ceramic electrodes present clear Tafel domains for overpotentials over 60 mV. Table 3 gives the OER Tafel parameters of each ceramic electrode. As it can be observed in the aforementioned table, both ceramic electrodes have the same Tafel slope (b): 240 mV·dec^{-1}. Consequently, the OER mechanism is the same in both cases. It should be noted that the observed Tafel slope is anomalously high. It is well-known that porous electrodes can present Tafel slopes as high as twice the Tafel slope of an analogue non-porous electrode (55). Therefore, the anomalously high Tafel slopes observed in this work are since the ceramic electrodes considered here behaves as porous electrodes. Furthermore, the actual Tafel slope is equal or higher to 120 mV·dec^{-1}. From this Tafel slope value, the following OER mechanism can be proposed for both, the (Sn,Sb)O_2 and the (Sn,Sb,Cu)O_2 electrodes (50) (Equations 2 to 7 in Appendix 1).

Where S denotes an active site on the surface of the electrode, · represents a chemical radical, and subscript *ads* refers to adsorbed intermediate species on the surface. Equation 3 is the rate-limiting reaction in this case, since the Tafel slope is equal or higher to 120 mV·dec^{-1} (56). This favors the accumulation of hydroxyl radicals (·OH), which is what is wanted in an EAOP anode.

Although the mechanism is the same in both ceramic electrodes, the kinetic parameters are not, as it can be deduced from the different values of the exchange current density (i_0): the (Sn,Sb,Cu)O_2 electrode has an exchange current density one order of magnitude lower than the

(Sn,Sb)O_2 electrode. This confirms the observations extracted from the CVs and the pseudo-steady-state polarization curve: the addition of CuO “inactivates” the electrode, improving it as EAOP anode. This is consistent with the results obtained by Brossard and Marquis (57) who already observed that the OER activity of copper was relatively low. Jaksic and co-workers proposed that the anomalously low OER activity of copper was due to the presence of electrons more than d^8 (58,59), which leads to a weaker electrode-OH interaction, which in turn leads to a lower OER activity. This explains why, adding copper to the (Sn,Sb)O_2 electrode deceases its OER activity, improving its performance as EAOP anode.

Finally, figure 12 compares the NOR degradation kinetics for the 3 considered anodes, at the same current density (i.e 80 $mA \cdot cm^{-2}$). It can be observed that for all 3 anodes, after 4 hours, NOR has been completely degraded. The fastest removal of NOR is obtained for the BDD anode followed by the ceramic (Sn,Sb,Cu)O_2 electrode. Figure 13 shows the evolution of TOC (i.e. proxy of the NOR mineralization) with time, for the 3 considered anodes. It can be observed that in all 3 cases, the TOC concentration decreases with time. The highest mineralization degree is achieved with the BDD electrode, while the ceramic (Sn,Sb,Cu)O_2 electrode is more efficient in terms of NOR mineralization than the (Sn,Sb)O_2 ceramic electrode, approaching mineralization values close to those obtained with the BDD electrode. These results are consistent with the results of the electrochemical characterization presented above, and confirm the observations extracted from the CVs, the pseudo-steady-state polarization curve and the Tafel plots: the addition of CuO “inactivates” the electrode, improving it as EAOP anode; thus, improving the degradation and mineralization of an organic compound (in this case, NOR).

4 Conclusions

The use of cooper oxide as sintering aid on a (Sb,Sn)O_2 electrodes processed by the traditional ceramic method has different effects over its properties depending on the added proportion. Densification and electrical resistivity increase with CuO content, but with different trends. That trends have in common a critical interval for CuO contents between 0.5 mol.% and 1.2 mol.%, where densification increases sharply, and resistivity shows a peak. This critical interval seems related with the transition from a porous microstructure of submicronic particles united trough

necks to a nearly full-densified microstructure of micron-sized grains with some isolated and rounded pores. A composition with 97.8 mol.% of SnO_2, 1.0 mol.% of Sb_2O_3 and 1.2 mol.% of CuO was considered a compromise between high densification (nearly zero open porosity) and low resistivity. The electrodes synthesized with this composition showed good mechanical properties and a resistivity around 1 Ω·cm, which allows its use as anode for electrooxidation processes.

The electrochemical characterization of this electrode showed that the addition of CuO as sintering aid significantly improves the electrochemical properties of the electrode as an EAOP anode with respect to the $(Sn,Sb)O_2$ electrode, at the expense of worsening its electrochemical roughness factor. The main electrochemical improvements of the addition of CuO are the widening of the electrochemical window and the increase of the “inactivity” of the electrode. The addition of CuO does not change the OER mechanism, but it does change the kinetic parameters, leading to a kinetic situation in which the accumulation of hydroxyl radicals is higher. This makes the selected $(Sn,Sb,Cu)O_2$ electrode better than the $(Sn,Sb)O_2$ electrode as an EAOP anode, as it was confirmed by NOR degradation tests.

Acknowledgements

The authors are very grateful to the Ministerio de Economia y Competitividad (Projects: CTQ2015-65202-C2-1-R and CTQ2015-65202-C2-2-R) and to the European Regional Development Fund (FEDER), for their economic support.

Appendix 1

Nomenclature

Roman letters

E	Electrode potential (V)
i	Current density $(A \cdot m^{-2})$
i_0	Exchange current density $(A \cdot m^{-2})$
OCP	Open circuit potential (V)
OEP	Oxygen evolution potential (V)

Greek letters

γ	Electrochemical rugosity factor
η	Overpotential (V)

Subscripts

a	Referred to active surface
g	Referred to geometric area

Equations

$\gamma = Q_{total}/Q_{out} = (Q_{out} + Q_{in})/Q_{out}$ Eq. (1)

$S + H_2O_{(l)} \leftrightarrow S(H_2O)_{ads}$ Eq. (2)

$S(H_2O)_{ads} \leftrightarrow S(\cdot OH)_{ads} + H^+_{(ac)} + e^-$ Eq. (3)

$S(\cdot OH)_{ads} \leftrightarrow S(\cdot O)_{ads} + H^+_{(ac)} + e^-$ Eq. (4)

$S(\cdot O)_{ads} + H_2O_{(l)} \leftrightarrow S(\cdot OOH)_{ads} + H^+_{(ac)} + e^-$ Eq. (5)

$S(\cdot OOH)_{ads} \leftrightarrow S(O_2)_{ads} + H^+_{(ac)} + e^-$ Eq. (6)

$S(O_2)_{ads} \leftrightarrow S + O_2$ Eq. (7)

5 Bibliography

1. Linares I., Martínez V. BC. Oxidation of persistent organic matter in industrial wastewater by electrochemical treatments. Avances en Ciencias e Ingeneria. 2011;2(1):21–36.
2. Chaplin BP. Critical review of electrochemical advanced oxidation processes for water treatment applications. Environ Sci Process Impacts. 2014;16(6):1182–203. https://doi.org/10.1039/c3em00679d.
3. Trellu C, Chaplin BP, Coetsier C, Esmilaire R, Cerneaux S, Causserand C, et al. Electro-oxidation of organic pollutants by reactive electrochemical membranes. Chemosphere. 2018;208:159–75. https://doi.org/10.1016/j.chemosphere.2018.05.026.
4. Trellu C, Coetsier C, Rouch JC, Esmilaire R, Rivallin M, Cretin M, et al. Mineralization of organic pollutants by anodic oxidation using reactive electrochemical membrane synthesized from carbothermal reduction of TiO_2. Water Res. 2018; 131:310–9. https://doi.org/10.1016/j.watres.2017.12.070.
5. Martínez-Huitle CA, Ferro S. Electrochemical oxidation of organic pollutants for the wastewater treatment: direct and indirect processes. Chem Soc Rev. 2006;35(12):1324–40. https://doi.org/10.1039/B517632H.
6. Kent CA, Concepcion JJ, Dares CJ, Torelli DA, Rieth AJ, Miller AS, et al. Water oxidation and oxygen monitoring by cobalt-modified fluorine-doped tin oxide electrodes. J Am Chem Soc. 2013; 135(23):8432–5. https://doi.org/10.1021/ja400616a.
7. Miranda MP, Del Rio R, Del Valle MA, Faundez M, Armijo F. Use of fluorine-doped tin oxide electrodes for lipoic acid determination in dietary supplements. J Electroanal Chem. 2012;668:1–6. https://doi.org/10.1016/j.jelechem.2011.12.022
8. Frasca S, Molero Milan A, Guiet A, Goebel C, Pérez-Caballero F, Stiba K, et al. Bioelectrocatalysis at mesoporous antimony doped tin oxide electrodes - Electrochemical characterization and direct enzyme communication. Electrochim Acta. 2013;110:172–80. https://doi.org/10.1016/j.electacta.2013.03.144
9. Evans CJ. Industrial uses of tin chemicals. In: Smith P.J. (eds). Chemistry of Tin. Springer Dordrecht (The Netherlands) 1998. p. 442–79. http://doi.org/10.1007/978-94-011-4938-9_12
10. Monrós G. El color de la cerámica : nuevos mecanismos en pigmentos para los nuevos

procesados de la industria cerámica. Publicacions de la Universitat Jaume I, Castellón, 2003.

11. Molera J, Pradell T, Salvado N, Vendrell-Saz M. Evidence of tin oxide recrystallization in opacified lead glazes. J Am Ceram Soc. 1999;82(10):2871–5. https://doi.org/10.1111/j.1151-2916.1999.tb02170.x.

12. Tsai PP, Chen IC, Tzeng MH. Tin oxide (SnO_X) carbon monoxide sensor fabricated by thick-film methods. Sensors Actuators B Chem. 1995;25(1–3):537–9. https://doi.org/ 10.1016/0925-4005(95)85116-X.

13. Li F, Xu J, Yu X, Chen L, Zhu J, Yang Z, et al. One-step solid-state reaction synthesis and gas sensing property of tin oxide nanoparticles. Sensors Actuators B. 2002;81:165–9. https://doi.org/10.1016/S0925-4005(01)00947-9.

14. Zuca S, Terzi M, Zaharescu M, Matiasovsky K. Contribution to the study of SnO_2-based ceramics. J Mater Sci. 1991;26(6):1673–6. https://doi.org/ 10.1007/BF00544681.

15. Batzill M, Diebold U. The surface and materials science of tin oxide. Prog Surf Sci. 2005;79(2–4):47–154. https://doi.org/ 10.1016/j.progsurf.2005.09.002.

16. Mora-Gómez J, García-Gabaldón M, Ortega E, Sánchez-Rivera MJ, Mestre S, Pérez-Herranz V. Evaluation of new ceramic electrodes based on Sb-doped SnO_2 for the removal of emerging compounds present in wastewater. Ceram Int. 2018;44(2):2216–22. https://doi.org/10.1016/j.ceramint.2017.10.178.

17. Leite ER, Cerri JA, Longo E, Varela JA, Paskocima CA. Sintering of ultrafine undoped SnO_2 powder. J Eur Ceram Soc. 2001; 21(5):669–75. https://doi.org/ 10.1016/S0955-2219(00)00250-8.

18. Scarlat O, Mihaiu S, Aldica G, Groza J, Zaharescu M. Semiconducting densified SnO_2-ceramics obtained by a novel sintering technique. J Eur Ceram Soc. 2004;24(6):1049–52. https://doi.org/ 10.1016/S0955-2219(03)00387-X.

19. Lin Y, Wu C. The Properties of antimony-doped tin oxide thin films from the sol-gel process. Surf Coatings Te. 1996;88:239–47. https://doi.org/ 10.1016/0257-8972(94)02393-X.

20. Garcia dos Santos IM, Longo E, Varela JA, Leite ER. Sintering of tin oxide processed by slip casting. J Eur Ceram Soc. 2000;20(14–15):2407–13. https://doi.org/10.1016/S0955-

2219(00)00130-8.

21. Krishnakumar T, Jayaprakash R, Pinna N, Phani AR, Passacantando M, Santucci S. Structural, optical and electrical characterization of antimony-substituted tin oxide nanoparticles. J Phys Chem Solids. 2009;70(6):993–9. http://.doi.org/10.1016/j.jpcs.2009.05.013

22. Medvedovski E. Tin oxide-based ceramics of high density obtained by pressureless sintering. Ceram Int. 2017;43(11):8396–405. https://doi.org/10.1016/j.ceramint.2017.03.185.

23. Scarlat O, Mihaiu S, Aldica G, Zaharescu M, Groza JR. Enhanced Properties of Tin(IV) Oxide Based Materials by Field-Activated Sintering. J Am Ceram Soc. 2003; 86(6):893–7. https://doi.org/10.1111/j.1151-2916.2003.tb03393.x.

24. Foschini CR, Perazolli L, Varela JA. Sintering of tin oxide using zinc oxide as a densification aid. J Mater Sci. 2004;39(18):5825–30. https://doi.org/10.1023/B:JMSC.0000040095.03906.61.

25. Mihaiu S, Scarlat O, Aldica G, Zaharescu M. SnO_2 electroceramics with various additives. 2001;21:1801–4. https://doi.org/10.1016/S0955-2219(01)00119-4.

26. Popescu AM, Mihaiu S, Zuca S. Microstructure and electrochemical behaviour of some SnO_2-based inert electrodes in aluminium electrolysis. Zeitschrift fur Naturforsch - Sect A J Phys Sci. 2002;57(1–2):71–5. https://doi.org/10.1515/zna-2002-1-210.

27. Rubenis K, Populoh S, Thiel P, Yoon S, Müller U, Locs J. Thermoelectric properties of dense Sb-doped SnO_2 ceramics. J Alloys Compd. 2017;692:515–21. http://.doi.org/10.1016/j.jallcom.2016.09.062.

28. Castro MS, Aldao CM. Characterization of SnO_2-varistors with different additives. J Eur Ceram Soc. 1998;18(14):2233–9. https://doi.org/10.1016/S0955-2219(97)00130-1.

29. Sahar MR, Hasbullah M. Properties of SnO_2-based ceramics. J Mater Sci. 1995;30(20):5304–6. https://doi.org/ 10.1007/BF00356085.

30. Nisiro D, Fabbri G, Celotti GC, Bellosi A. Influence of the additives and processing conditions on the characteristics of dense SnO_2 -based ceramics. J. Mat. Sci. 2003; 38(12):2727–42. https://doi.org/10.1023/A:1024459307992.

31. German RM. Sintering theory and practice. John Wiley & Sons, Inc; New York, 1996: p

11-12.

32. Giner-Sanz JJ, Ortega EM, Pérez-Herranz V. Experimental Quantification of the Effect of Nonlinearities on the EIS Spectra of the Cathodic Electrode of an Alkaline Electrolyzer. Fuel Cells. 2017; 17(3):391–401. https://doi.org/10.1002/fuce.201600137.

33. Giner-Sanz JJ, Ortega EM, Pérez-Herranz V. Mechanistic equivalent circuit modelling of a commercial polymer electrolyte membrane fuel cell. J Power Sources. 2018; 379:328–37. https://doi.org/ 10.1016/j.jpowsour.2018.01.066.

34. Orazem ME, Tribollet B. Electrochemical Impedance Spectroscopy. John Wiley & Sons; Hoboken, New Jersey, 2011.

35. Agarwal P, Orazem ME, Garcia-Rubio LH. Application of Measurement Models to Impedance Spectroscopy III. Evaluation of Consistency with the Kramers-Kronig Relations. J. Electrochem. Soc. 1995; 142 (12):4159-4168. https://doi.org/ 10.1149/1.2048479.

36. Giner-Sanz JJ, Ortega EM, Pérez-Herranz V. Total harmonic distortion based method for linearity assessment in electrochemical systems in the context of EIS. Electrochim Acta. 2015;186:598–612.https:/doi.org/10.1016/j.electacta.2015.10.152.

37. Giner-Sanz JJ, Ortega EM, Pérez-Herranz V. Harmonic analysis based method for linearity assessment and noise quantification in electrochemical impedance spectroscopy measurements: Theoretical formulation and experimental validation for Tafelian systems. Electrochimica Acta. 2016; 211:1076-1091. https://doi.org/10.1016/j.electacta.2016.06.133.

38. Giner-Sanz JJ, Ortega EM, Pérez-Herranz V. Montecarlo based quantitative Kramers–Kronig test for PEMFC impedance spectrum validation. Int J Hydrogen Energy. 2015; 40(34):11279–93. https://doi.org/10.1016/j.ijhydene.2015.03.135.

39. Giner-Sanz JJ, Ortega EM, Pérez-Herranz V. Application of a Montecarlo based quantitative Kramers-Kronig test for linearity assessment of EIS measurements. Electrochim Acta. 2016; 209:254–68. https://doi.org/10.1016/j.electacta.2016.04.131.

40. Giner-Sanz JJ, Ortega EM, Pérez-Herranz V. Optimization of the electrochemical impedance spectroscopy measurement parameters for PEM fuel cell spectrum determination. Electrochim Acta. 2015; 174:1290–8.

https://doi.org/10.1016/j.electacta.2015.06.106.

41. Giner-Sanz JJ, Ortega EM, Pérez-Herranz V. Hydrogen crossover and internal short-circuit currents experimental characterization and modelling in a proton exchange membrane fuel cell. Int J Hydrogen Energy. 2014; 39(25):13206–16. https://doi.org/10.1016/j.ijhydene.2014.06.15.

42. Giner-Sanz JJ, Ortega EM, Pérez-Herranz V. Statistical Analysis of the Effect of the Temperature and Inlet Humidities on the Parameters of a PEMFC Model. Fuel Cells. 2015; 15(3):479–93. https://doi.org/10.1002/fuce.201400163.

43. Giner-Sanz JJ, Ortega EM, Pérez-Herranz V. Optimization of the Perturbation Amplitude for Impedance Measurements in a Commercial PEM Fuel Cell Using Total Harmonic Distortion. Fuel Cells. 2016; 16(4):469–79. https://doi.org/10.1002/fuce.201500141.

44. Giner-Sanz JJ, Ortega EM, Pérez-Herranz V. Harmonic Analysis Based Method for Perturbation Amplitude Optimization for EIS Measurements. J Electrochem Soc. 2017; 164(13):H918–24. Available from: https://doi.org/10.1149/2.1451713jes.

45. Giner-Sanz JJ, Ortega EM, Pérez-Herranz V. Statistical analysis of the effect of temperature and inlet humidities on the parameters of a semiempirical model of the internal resistance of a polymer electrolyte membrane fuel cell. J Power Sources. 2018; 381:84–93. https://doi.org/ 10.1016/j.jpowsour.2018.01.093.

46. Hrbac J, Halouzka V, Trnkova L, Vacek J. eL-Chem Viewer: A Freeware Package for the Analysis of Electroanalytical Data and Their Post-Acquisition Processing. Sensors. 2014; 14(8):13943–54. https://doi.org/ 10.3390/s140813943.

47. Stan M, Mihaiu S, Crisan D, Zaharescu M. Subsolidus phase equilibrium in the Cu-Sb-O system. Eur J Solid State Inorg Chem. 1998;35(3):243–54. https://doi.org/10.1016/S0992-4361(98)80005-2

48. Lalande Ã, Ollitrault-fichet R, Boch P. Sintering behaviour of CuO-doped SnO_2. J Eur Ceram Soc. 2000; 20 (14-15) :2415-2420. Available from https://doi.org/10.1016/S0955-2219(00)00153-9.

49. Zhang TS, Kong LB, Song XC, Du ZH, Xu WQ, Li S. Densification behaviour and sintering mechanisms of Cu- or Co-doped SnO_2: A comparative study. Acta Mater. 2014;62(1):81–8. https:doi.org/ 10.1016/j.actamat.2013.09.031.

50. García-Osorio DA, Jaimes R, Vazquez-Arenas J, Lara RH, Alvarez-Ramirez J. The Kinetic Parameters of the Oxygen Evolution Reaction (OER) Calculated on Inactive Anodes via EIS Transfer Functions: $^{\bullet}$OH Formation. J Electrochem Soc. 2017;164(11):E3321–8. https://doi.org/10.1149/2.0321711jes.

51. Ardizzone S, Fregonara G, Trasatti S. “Inner” and “outer” active surface of RuO_2 electrodes. Electrochim Acta. 1990; 35(1):263–7. https://doi.org/10.1016/0013-4686(90)85068-X

52. Reier T, Oezaslan M, Strasser P. Electrocatalytic Oxygen Evolution Reaction (OER) on Ru, Ir, and Pt Catalysts: A Comparative Study of Nanoparticles and Bulk Materials. ACS Catal. 2012; 2(8):1765–72. https://doi.org/10.1021/cs3003098.

53. Kötz R, Stucki S, Carcer B. Electrochemical waste water treatment using high overvoltage anodes. Part I: Physical and electrochemical properties of SnO_2 anodes. J Appl Electrochem. 1991; 21(1):14–20. https://doi.org/10.1007/BF01103823.

54. Comninellis C. Electrocatalysis in the electrochemical conversion/combustion of organic pollutants for waste water treatment. Electrochim Acta. 1994; 39(11–12):1857–62. https://doi.org/10.1016/0013-4686(94)85175-1.

55. Jeff N. Soderberg, Anne C. Co, Aislinn H. C. Sirk and, Birss* VI. Impact of Porous Electrode Properties on the Electrochemical Transfer Coefficient. J. Phys. Chem. B, 2006; 110(21): 10401–10410. https://doi.org/10.1021/jp060372f.

56. Liu B, Wang C, Chen Y. Surface determination and electrochemical behavior of IrO_2-RuO_2-SiO_2 ternary oxide coatings in oxygen evolution reaction application. Electrochim Acta. 2018; 264:350–7. https://doi.org/ 10.1016/j.electacta.2018.01.141.

57. Brossard L, Marquis B. Electrocatalytic behavior of Co/Cu electrodeposits in 1M KOH at 30°C. Int J Hydrogen Energy. 1994; 19(3):231–7. https://doi.org/ 10.1016/0360-3199(94)90091-4.

58. Jaksic JM, Ristic NM, Krstajic N V., Jaksic MM. Electrocatalysis for hydrogen electrode reactions in the light of fermi dynamics and structural bonding FACTORS—I. individual electrocatalytic properties of transition metals. Int J Hydrogen Energy. 1998;23(12):1121–56. https://doi.org/ 10.1016/S0360-3199(98)00014-7.

59. Fazle Kibria AKM, Tarafdar SA. Electrochemical studies of a nickel–copper electrode for

the oxygen evolution reaction (OER). Int J Hydrogen Energy. 2002; 27(9):879–84. https://doi.org/ 10.1016/S0360-3199(01)00185-9.

Figures

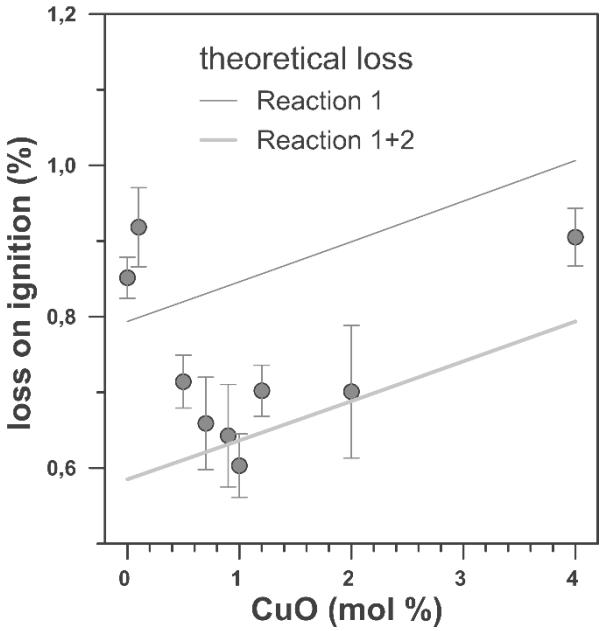

Figure 1. Loss of ignition of sintered electrodes as a function of molar percentage of copper oxide in their composition.

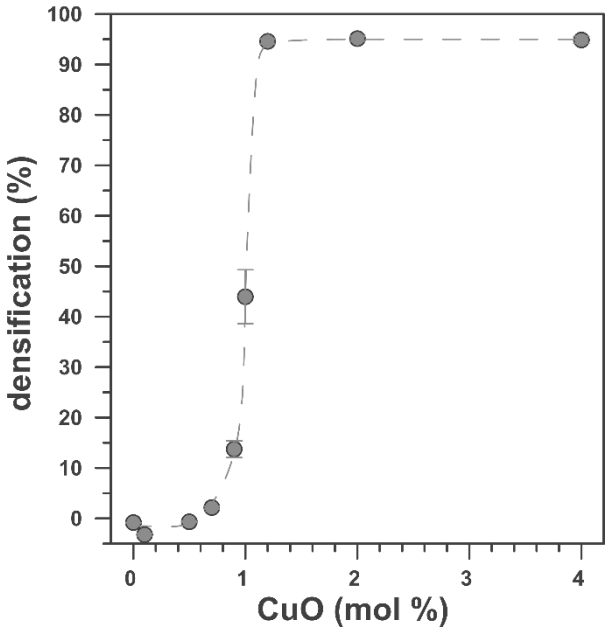

Figure 2. Densification of sintered electrodes as a function of molar percentage of copper oxide in their composition.

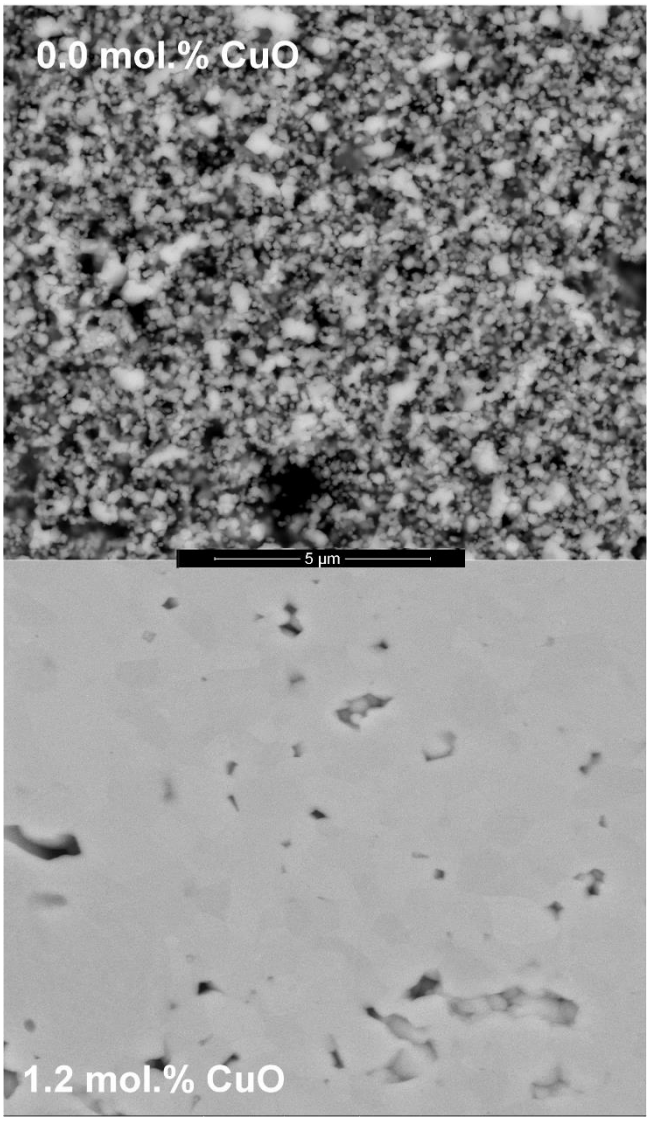

Figure 3. Microstructure comparison between sintered specimens of the composition without CuO (upper) and the one with 1.2 mol.% of CuO (down) as sintering aid.

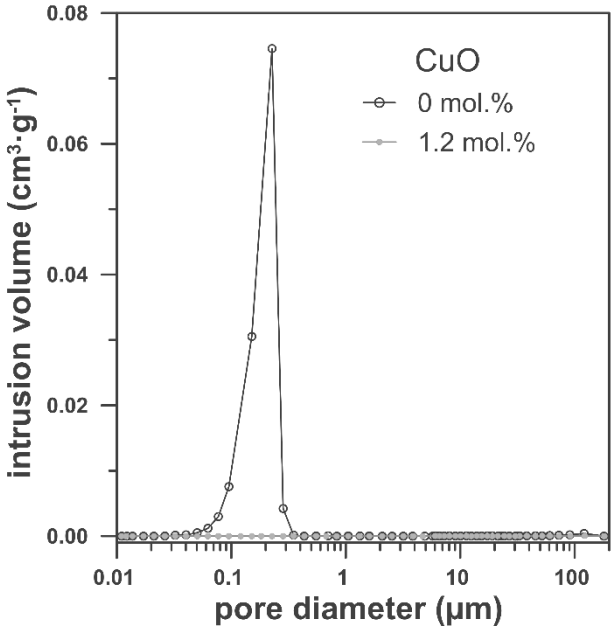

Figure 4. Total pore volume distribution comparison between sintered specimens of the composition without CuO and the one with 1.2 mol.% of CuO as sintering aid.

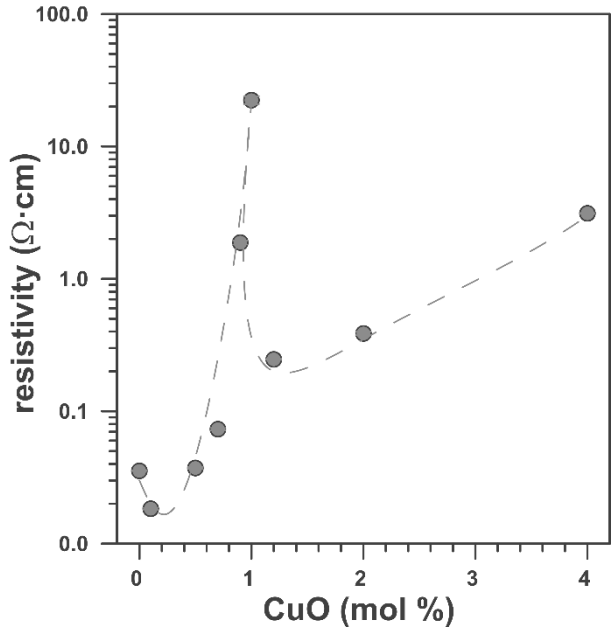

Figure 5. Resistivity of sintered electrodes as a function of the percentage of CuO.

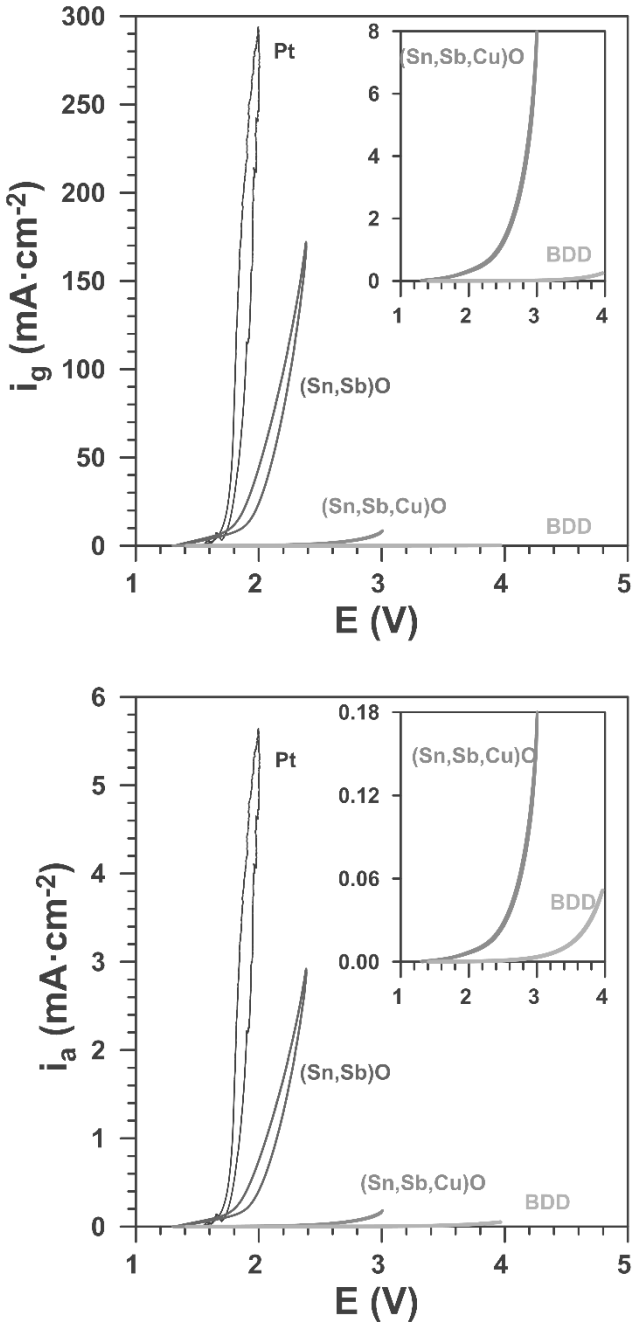

Figure 6.a. I-R corrected cyclic voltammetry obtained at a scan rate of 100 mV·s^{-1} and referred to geometric area (upper) and to active surface area (down).

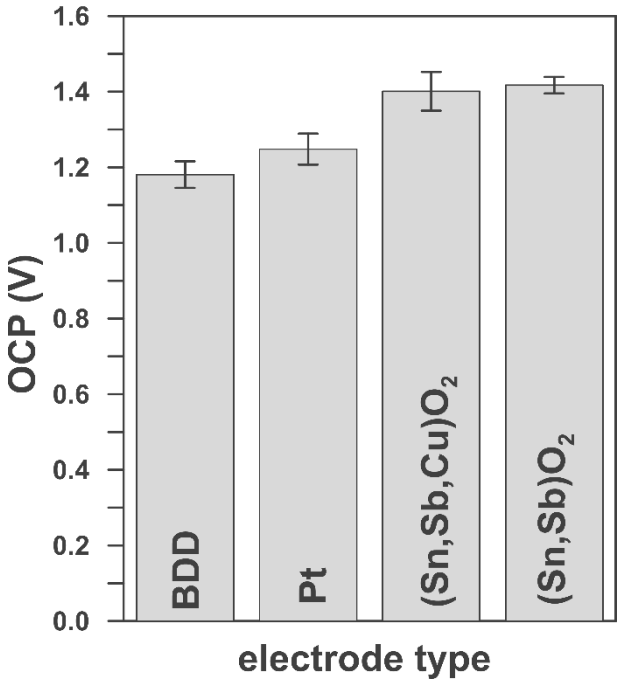

Figure 7. Open circuit voltage of the different electrodes.

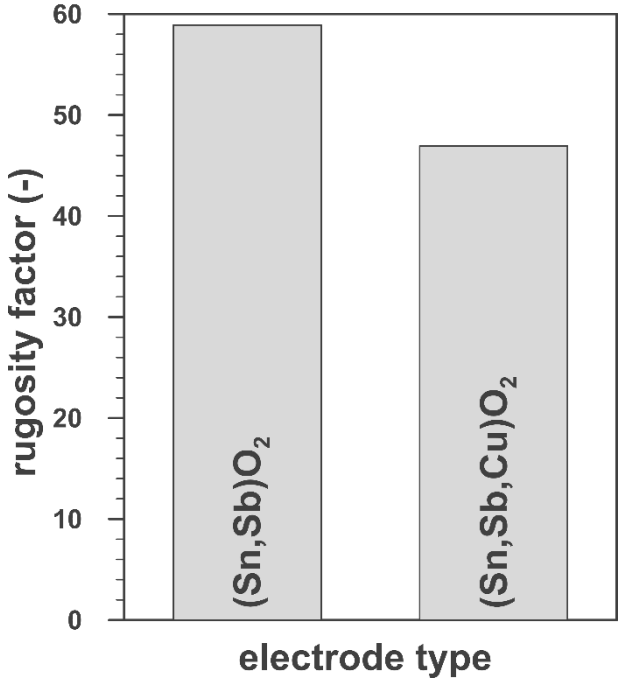

Figure 8. Electrochemical rugosity factor of the two ceramic electrodes.

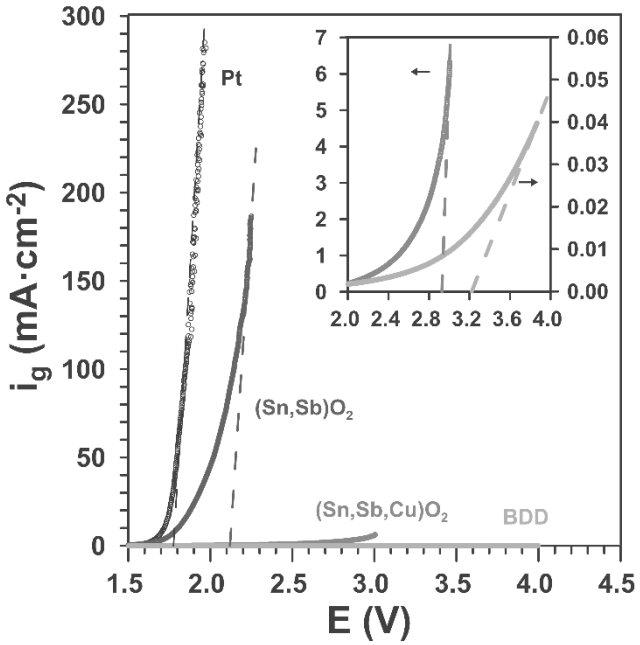

Figure 9. I-R corrected pseudo-steady-state polarization curves of the electrodes.

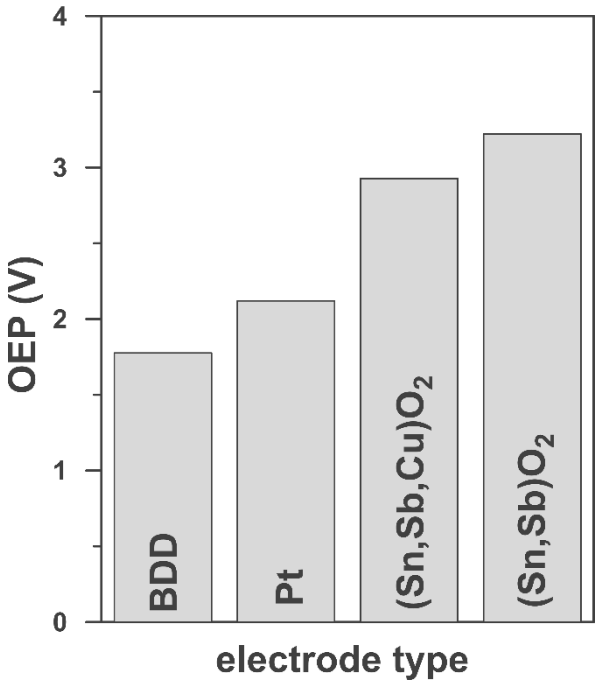

Figure 10. Oxygen evolution potential of the different electrodes.

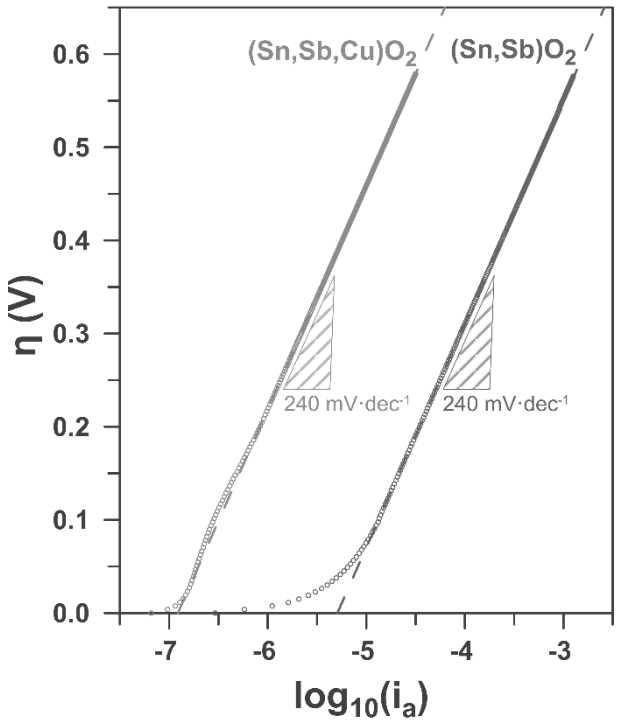

Figure 11. Tafel plot

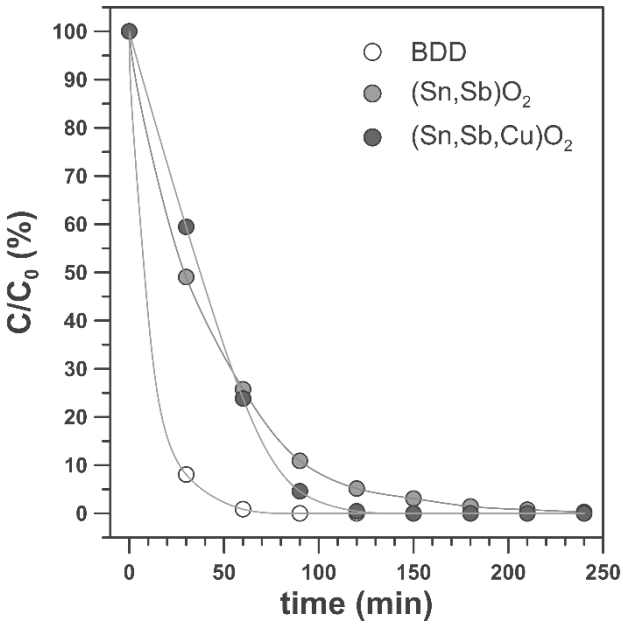

Figure 12. Effect of the electrode material on the decay of the relative NOR concentration as a function of time.

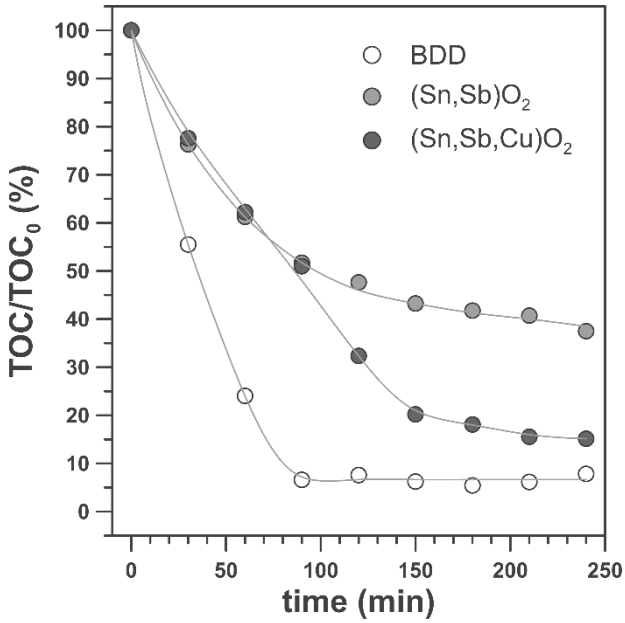

Figure 13. Effect of the electrode material on the decay of the relative TOC concentration as a function of time.

Tables

Table 1. Formulated compositions (mol.%)

Composition	SnO_2	Sb_2O_3	CuO
A	99.0	1.0	0.0
B	98.9	1.0	0.1
C	98.5	1.0	0.5
D	98.3	1.0	0.7
E	98.1	1.0	0.9
F	97.0	1.0	1.0
G	97.8	1.0	1.2
H	97.0	1.0	2.0
I	95.0	1.0	4.0

Table 2. Total pore volume comparison between sintered specimens from A and G compositions.

Composition	CuO (mol.%)	Total pore volume (cm^3/g)
A	0.0	0.133
G	1.2	0.000

Table 3. Oxygen evolution reaction Tafel parameters.

Electrode	b ($mV \cdot dec^{-1}$)	i_0 ($A \cdot cm_a^{-2}$)
$(Sn,Sb)O_2$	240	5.08×10^{-6}
$(Sn,Sb,Cu)O_2$	240	1.23×10^{-7}